Anomalous Dirac Plasmons in 1D Topological Electrides

Jianfeng Wang,[1] Xuelei Sui,[2,1] Shiwu Gao,[1] Wenhui Duan,[2,4] Feng Liu,[3,4,*] and Bing Huang[1,†]
[1]Beijing Computational Science Research Center, Beijing 100193, China
[2]Department of Physics and State Key Laboratory of Low-Dimensional Quantum Physics, Tsinghua University, Beijing 100084, China
[3]Department of Materials Science and Engineering, University of Utah, Salt Lake City, Utah 84112, USA
[4]Collaborative Innovation Center of Quantum Matter, Beijing 100084, China

(Received 1 April 2019; published 12 November 2019)

The plasmon opens up the possibility to efficiently couple light and matter at subwavelength scales. In general, the plasmon frequency, intensity, and damping are dependent on the carrier density. These dependencies, however, are disadvantageous for stable functionalities of plasmons and render fundamentally a weak intensity at low frequency, especially for the Dirac plasmon (DP) widely studied in graphene. Here we demonstrate a new type of DP, emerging from a Dirac nodal-surface state, which can simultaneously exhibit a *density-independent* frequency, intensity, and damping. Remarkably, we predict the realization of anomalous DP (ADP) in 1D topological electrides, such as Ba_3CrN_3 and Sr_3CrN_3, by first-principles calculations. The ADPs in both systems have a density-independent frequency and high intensity, and their frequency can be tuned from terahertz to midinfrared by changing the excitation direction. Furthermore, the intrinsic weak electron-phonon coupling of anionic electrons in electrides affords an added advantage of low-phonon-assisted damping and hence a long lifetime of the ADPs. Our Letter paves the way to developing novel plasmonic and optoelectronic devices by combining topological physics with electride materials.

DOI: 10.1103/PhysRevLett.123.206402

The plasmon, resulting from collective electron density oscillations, dominates the long-wavelength elementary excitation spectrum in metals and doped semiconductors [1]. It enables efficient coupling of light and matter at subwavelength scales, opening up the possibility of manipulating electromagnetic energy in nanophotonic and optoelectronic devices [1–7]. Recently, Dirac plasmons (DPs), as prototyped in graphene, have attracted great interest because of their tunable frequency, enhanced light confinement, and long lifetime [8–10]. The typical terahertz or infrared (IR) response of a DP gives rise to promising applications in spectroscopy, biosensing, and security-related areas [8–14].

To date, all the well-known plasmons have a common feature: a strong dependence on carrier density (n), which manifests in three ways. First, their *frequency* strongly depends on n. For example, the long-wavelength plasmon frequency ω in metals and graphene follows the $n^{1/2}$ and $n^{1/4}$ power-law scaling [10,11], respectively. Although this dependence can facilitate a gate-voltage tunability, e.g., in a graphene plasmon [10–14], it is disadvantageous for efficient plasmon-enhanced photovoltaics, photocatalysis, and photodetections that require a stable excitation frequency in changeable environments. Secondly, the plasmon *intensity* is dependent on n (here the plasmon intensity refers to the loss function) because the density of states (DOS) near the Fermi level (E_F) is usually related to n (e.g., DOS $\sim n^{1/3}$, $n^{1/2}$ for 3D metals and graphene, respectively) [15]. This results in a weak plasmon intensity at low frequency. Third, the plasmon *damping* is related to n (the phonon-assisted damping is dominant for low-frequency DPs, as discussed later) [31,38]. This dependence can make the damping ultralow at low carrier density; e.g., a lifetime of picoseconds for a graphene plasmon was achieved [32,33], but it will inevitably result in a rapid decrease of plasmon lifetime as the carrier density increases [31,38].

In this Letter, we demonstrate an anomalous DP (ADP), emerging from a unique Dirac nodal-surface (DNS) state, which exhibits surprisingly n-independent frequency, intensity, and damping. Remarkably, we predict the existence of ADP in 1D topological electrides, where the DNS states are formed by anionic electrons trapped in the cavities. In addition, the loosely bound anionic electrons in electrides result in an ultraweak phonon scattering and hence a long lifetime of the ADPs. Importantly, we discover that Ba_3CrN_3 and Sr_3CrN_3 are ideal 1D topological electrides to realize the ADPs, having a tunable frequency from terahertz to mid-IR and a density-independent low-phonon-assisted damping for a long lifetime.

The classical long-wavelength plasmon frequency in 3D metals is known as $\hbar\omega_{\mathrm{PM}} = (4\pi e^2 n/\kappa m)^{1/2}$, where m and κ are effective mass and the dielectric constant, respectively. Recently, the topological semimetal (TSM) states [39–42], characterized by a linear band crossing between conduction and valence bands in higher dimensions

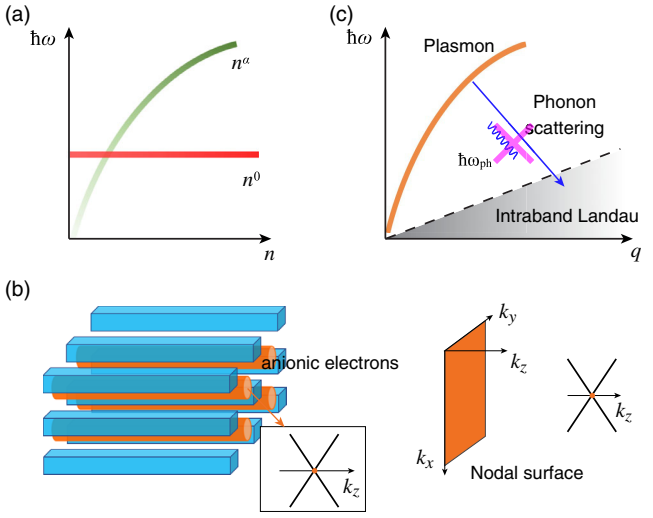

FIG. 1. (a) Density dependences of plasmon frequency and intensity. (Green curve) The usual plasmon following a $\omega \sim n^\alpha$ scaling ($\alpha = 1/2, 1/3, 1/4$ for parabolic metals, DNP, and DNL semimetals, respectively). (Red curve) Our proposed ADP following the $\omega \sim n^0$ scaling. The brightness of the color indicates the intensity of the plasmon [15]. (b) (Left) Schematic plot for 1D electride, where the orange channels denote the anionic electrons. (Inset) A band crossing of a single anionic electron chain along the k_z direction. (Right) The crossing points form a 2D degenerate DNS. (c) Schematic illustration of the phonon-assisted damping for the Dirac plasmon. The plasmon may enter the intraband Landau region and decay into electron-hole pairs via phonon scattering or by emitting a phonon. This damping pathway is naturally suppressed in electrides.

(i.e., 1D and 2D), have provided a platform to create novel DPs beyond graphene [16,17,43,44]. For a TSM, the "relativistic" effective mass of quasiparticles is n dependent, as $m_r \propto n^{1/3}$ and $n^{1/2}$ for Dirac nodal point (DNP) and Dirac nodal line (DNL), respectively [15]. Consequently, the $n^{1/2}$ scaling in the classical plasmon frequency is partially offset by m_r, resulting in $\omega_{\mathrm{DNP}} \sim n^{1/3}$ and $\omega_{\mathrm{DNL}} \sim n^{1/4}$ for DNP and DNL, respectively [16,17,43]. Interestingly, we realize when the dimensionality of band crossing is further increased to 2D DNS [45,46], m_r becomes proportional to n, to completely offset the $n^{1/2}$ scaling in the frequency. Consequently, the plasmon frequency of a DNS semimetal becomes independent of n, fundamentally different from all the known plasmons [see Fig. 1(a)].

Using the dynamical dielectric function based on random phase approximation (RPA) [15] and the Lindhard function of Dirac systems [16], one can obtain the noninteracting irreducible polarizability of DNS in the long-wavelength limit as

$$\Pi(\boldsymbol{q}, \omega) = \frac{gS\hbar v_F q^2 \cos^2\theta}{4\pi^3\omega^2} + O(q^4/\omega^4), \qquad (1)$$

where g is the degeneracy factor, S is the DNS area, v_F is the Fermi velocity along the normal direction of DNS, and θ is the angle between $\boldsymbol{q}$ and the normal direction of DNS. One then deduces the long-wavelength plasmon frequency as [15]

$$\hbar\omega_{\mathrm{DNS}} = \sqrt{\frac{ge^2 S\hbar v_F \cos^2\theta}{\pi^2\kappa}} + O(q^2). \qquad (2)$$

As shown by the red line in Fig. 1(a), the long-wavelength plasmon of DNS exactly follows $\omega_{\mathrm{DNS}} \sim n^0$. Moreover, the DNS has a constant high DOS near E_F [15], which produces a constant strong plasmon intensity. Consequently, an ADP has an inherently n-independent frequency and high intensity. As indicated by Eq. (2), the frequency of ADP depends solely on the direction of plasmon excitation (a $|\cos\theta|$ function), providing a simple way to continuously tune its frequency. In addition, the n-independent DOS makes the phonon-assisted damping of ADP immune to carrier density, as discussed later.

Though the DNS states were proposed theoretically [45,46], they have not been observed in experiments due to the lack of ideal materials. Here we predict that the DNS states and ADPs can be realized in 1D topological electrides. Electrides are known as special ionic solids, in which excess electrons trapped in the cavities serve as anions [47–50]. They are classified into 0D, 1D, and 2D electrides according to the dimensionality of confinement [51]. The anionic electrons with low work function may appear as occupied states near E_F, suitable for band crossing [52]. As shown in Fig. 1(b), when the anionic electrons are confined in 1D channels (e.g., z direction), they may generate a band crossing along the k_z direction. Their interchannel coupling in a periodic array translates the crossing points along the k_x and k_y directions in the 3D Brillouin zone (BZ). The resulting 2D band crossing can be protected by some specific crystal symmetries to realize a DNS state. In addition, there is a negligible spin-orbit coupling (SOC) for loosely bound anionic electrons, which is vital for achieving the spinless nodal states.

We note that the nature of electrides also naturally makes the excited ADP have a low damping. In general, there are several possible damping pathways for plasmons [53], including direct decay into electron-hole pairs via intra- or interband Landau damping, scattering from impurities or defects, and inelastic scattering with phonons. For DPs, the first two processes can be effectively reduced by changing n and improving sample quality, and the phonon-assisted damping is usually the dominant loss pathway [31,53,54]. As shown in Fig. 1(c), a DP can decay into an electron-hole pair via emission of a phonon. Here for our proposed ADPs in electrides, the loosely bound anionic electrons generally exhibit a weak electron-phonon (e-ph) coupling [55], leading to a largely suppressed phonon-assisted damping pathway.

The above analysis indicates that an ADP generated by a DNS state in 1D electrides could realize a density-independent frequency, high intensity, and low damping. Based on an

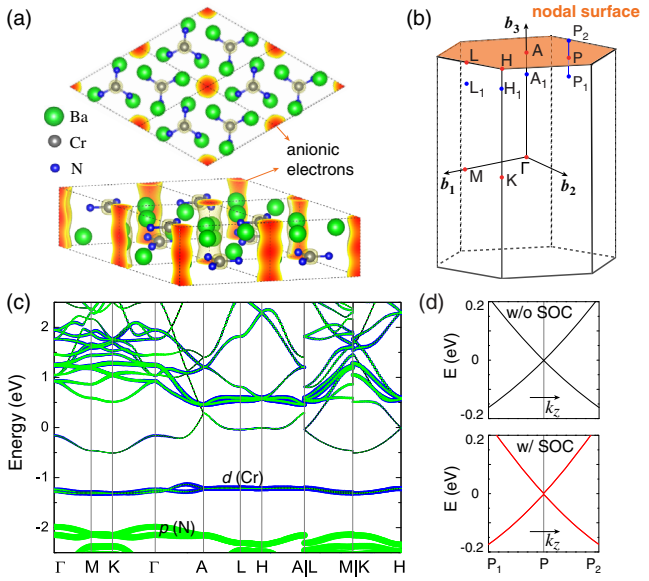

FIG. 2. (a) Top (upper) and side (lower) view of the crystal structure of Ba_3CrN_3. (b) The first BZ of Ba_3CrN_3. The high-symmetry and some arbitrary points (dots) are labeled. (c) Band structure with atomic orbital projections. The Fermi level is set to zero. The partial charge density distribution for the energy bands around E_F (−0.3–0.3 eV) are depicted by the red regions in (a). (d) Magnified band structure along an arbitrary line P_1–P–P_2 perpendicular to the $k_z = \pi/c$ plane at an arbitrary P point located in the plane, as indicated in (b). The nodal surface in momentum space is plotted by the orange plane ($k_z = \pi/c$) in (b).

extensive structural search in the Inorganic Crystal Structure Database, we successfully identify that Ba_3CrN_3 and Sr_3CrN_3 are ideal 1D electrides to realize the desired ADP.

Ba_3CrN_3 and Sr_3CrN_3 have already been synthesized in experiments [23]. Here we take Ba_3CrN_3 as an example to illustrate its ADP excitations and leave the results of Sr_3CrN_3 for the Supplemental Material [15]. As shown in Fig. 2(a), the unit cell of hexagonal Ba_3CrN_3 (space group $P6_3/m$) contains two trigonal planar CrN_3 anions that are related to each other by an inversion or screw rotation symmetry [23]. Along the z direction, a 1D cavity is formed at the corner of the unit cell. Our calculations indicate that Ba_3CrN_3 is nonmagnetic, because Cr has a +4 charge state and its remaining two d electrons fill a singlet state. Thus, there are two "excess" electrons per unit cell to act as "anions." The band structure is shown in Fig. 2(c), indicating a semimetal. Strikingly, the two energy bands near E_F are mostly contributed to by the anionic electrons with negligible atomic orbital components. The band dispersions are small in the $k_z = 0$ and $k_z = \pi/c$ planes but large along the k_z direction, indicating a 1D nature. The partial charge densities of these two bands around E_F further show that the anionic electrons are confined in the 1D cavity [Fig. 2(a)].

Figure 2(c) shows that the conduction and valence bands are degenerate along the high-symmetry paths A–L–H–A, but split along Γ–A, M–L, and K–H. Actually, such band degeneracy occurs at all points in the $k_z = \pi/c$ plane, as confirmed by plotting the bands [Fig. 2(d)] along an arbitrary line P_1–P–P_2 perpendicular to the $kz = \pi/c$ plane at an arbitrary P point in the plane [see Fig. 2(b)]. So, the band crossing takes place throughout the BZ boundary to form a perfect DNS state [orange plane in Fig. 2(b)]. It is noted that the DNS near E_F is not completely flat due to a small interchannel coupling.

The DNS state is protected by a nonsymmorphic symmetry [15,45]. Ba_3CrN_3 has time-reversal symmetry $T = K$, with K being the complex conjugation, inversion symmetry I, and screw rotation symmetry $S_z = \{C_{2z}|c/2\}$. Two compound symmetries, IT and IS_z, are preserved in the $k_z = \pi/c$ plane, and their anticommutation ensures a twofold band degeneracy in the entire $k_z = \pi/c$ plane [15,45]. When SOC effect is included, this degeneracy is lifted but the SOC gap is negligibly small due to the unique nature of anionic electrons [see Fig. 2(d)]. Similar conclusions are drawn for Sr_3CrN_3 [15].

After establishing an ideal DNS state in Ba_3CrN_3, we investigate its plasmonic excitations. Under RPA, the collective plasmon mode can be determined by the dynamical dielectric function $\epsilon(\boldsymbol{q},\omega) = 1 - V(q)\Pi(\boldsymbol{q},\omega)$, where $V(q) = 4\pi e^2/\kappa q^2$. In the long-wavelength limit ($q \to 0$), a noninteracting irreducible polarizability is given by [16,56]

$$\Pi(\boldsymbol{q},\omega) = -\frac{2}{(2\pi)^3}\int d^3\boldsymbol{k}\sum_{l,l'}|\langle \boldsymbol{k}+\boldsymbol{q},l'|e^{i\boldsymbol{q}\cdot\boldsymbol{r}}|\boldsymbol{k},l\rangle|^2 \times \frac{n_F(E_{\boldsymbol{k},l}) - n_F(E_{\boldsymbol{k}+\boldsymbol{q},l'})}{\hbar\omega + E_{\boldsymbol{k},l} - E_{\boldsymbol{k}+\boldsymbol{q},l'} + i\eta}, \quad (3)$$

where n_F is the Fermi-Dirac distribution function and η is the broadening of the plasmon mode. The collective plasmon mode is defined at zeros of the complex dynamical dielectric function. It is more convenient to calculate the electron energy loss spectrum (EELS), i.e., $\mathrm{EELS} = -\mathrm{Im}[1/\epsilon(\boldsymbol{q},\omega)]$, whose broadened peaks indicate the plasmons [56]. Along the z direction, we calculate the long-wavelength ($q = 0.001$ Å^{-1}) dielectric function of Ba_3CrN_3 and the EELS at $T = 300$ K, as shown in Fig. 3(a). A sharp plasmon peak with high intensity appears for $\mathrm{Re}[\epsilon(\boldsymbol{q},\omega)] = 0$. Simultaneously, the $\mathrm{Im}[\epsilon(\boldsymbol{q},\omega)] \to 0$, indicating a weak direct damping rate. The plasmon excitation energy of 0.125 eV corresponds to a frequency of ∼30 THz in the mid-IR range. As shown in Fig. 3(b), the parabolic plasmon dispersion (3D dielectric screening) lies above the region of intraband Landau damping, consistent with the sharp peak of plasmon; it indicates that the direct decay into electron-hole pairs is almost forbidden.

In Fig. 3(c), we plot the plasmon frequency versus n and excitation direction angle θ at the long-wavelength limit. Remarkably, at any fixed excitation direction, the plasmon frequency keeps a constant value ($\omega \sim n^0$) for a significantly

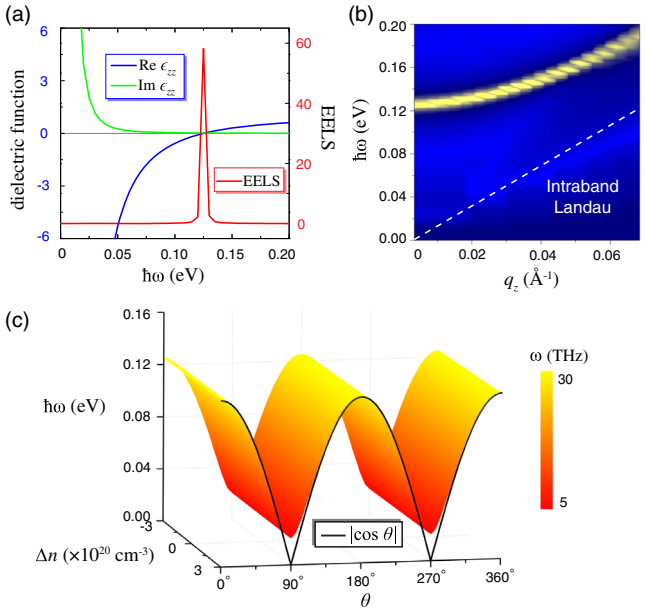

FIG. 3. (a) Real and imaginary parts of dielectric function and EELS of Ba_3CrN_3 as functions of frequency with $q = 0.001$ Å^{-1} along the z direction. (b) EELS as a function of frequency $\hbar\omega$ and wave vector q_z. The white dashed line denotes the upper edge $\hbar v_F q$ of the intraband particle-hole continuum. (c) Plasmon frequency as a function of Δn and excitation direction (θ). The color from red to yellow indicates the frequency from terahertz to mid-IR, and the brightness of color indicates almost a constant high plasmon intensity.

large range of n up to $\sim 3 \times 10^{20}$ cm^{-3} (i.e., within the energy range of linear band dispersion [15]), consistent with our predicted feature of ADP. Meanwhile, the high intensity of ADP remains almost unchanged for different n [15] because of a constant DOS within the same energy range. On the other hand, the ADP frequency depends on θ and can be continuously tuned, following a $|\cos\theta|$ function [black curve in Fig. 3(c)], which agrees well with our model [Eq. (2)]. It is noted that the plasmon mode along the x direction (i.e., $\theta = 90°$) has a small excitation energy ($\sim$20 meV) and enters the particle-hole continuum at large q [15], whereas the nonzero frequency for $\theta = 90°$ is due to a small dispersion in the xy plane of the DNS band. Moreover, the high intensity of ADP is almost maintained for different θ, as confirmed by our calculations [15]. Thus, by changing θ, a high-intensity ADP with a frequency tuned from terahertz to mid-IR can be achieved [Fig. 3(c)]. It is noted that the realization of n-independent ADP requires two conditions: 1D Dirac spectrum ($\sim$30 meV near E_F for Ba_3CrN_3) and a long-wavelength limit. Once the plasmon frequency reaches the quadratic dispersion region, it becomes n dependent. The 2D classical plasma also has n-independent DOS and hence high intensity, but its frequency is n dependent ($\omega \sim n^{1/2}$), differing from ADP. In addition, we find the ADP frequency is robust against strain, due to the nature of loosely bound anionic electrons [15].

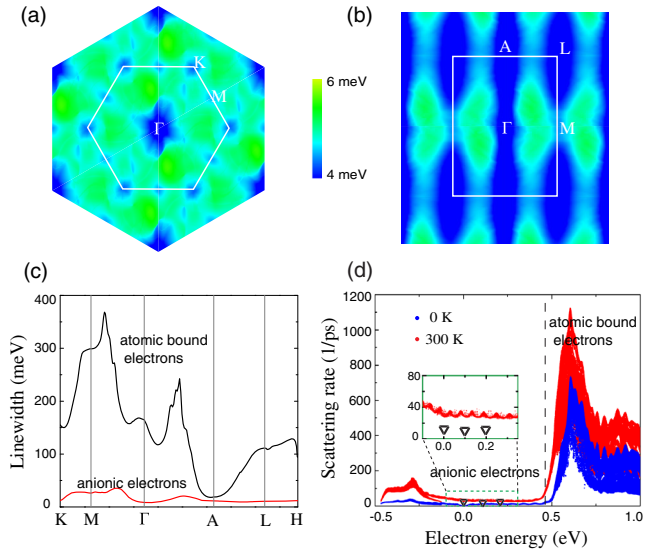

FIG. 4. Average e-ph coupling matrix element $|g_{mn,\nu}(\boldsymbol{k},\boldsymbol{q})|$ of all 42 phonon modes for the DNS band of Ba_3CrN_3 at the A point of BZ versus phonon wave vector $\boldsymbol{q}$ in the (a) $q_z = 0$ and (b) $q_x = 0$ plane. (c) Electron linewidth for the DNS band of anionic electrons (red line) and the higher band of atomic bound electrons (black line) along high-symmetry $\boldsymbol{k}$ points. (d) Scattering rate of electron versus energy at 0 K (blue dots) and 300 K (red dots), respectively. The Fermi level is set to zero. The three black triangles in (d) and enlarged view in the inset are the calculated data of phonon-assisted plasmon damping rate at 300 K, indicating that plasmon damping rates are lower than scattering rates (see Refs. [27,57–60] for details).

Finally, we discuss the phonon scattering of ADPs in Ba_3CrN_3, by calculating the e-ph interaction for the DNS states. The electron linewidth or scattering rate is directly connected to the imaginary part of the e-ph self-energy [28]

$$\Sigma''_{n,\boldsymbol{k}} = \pi \sum_{m\nu\boldsymbol{q}} |g_{nm\nu}(\boldsymbol{k},\boldsymbol{q})|^2 \times [(N^0_{\nu\boldsymbol{q}} + f^0_{m\boldsymbol{k}+\boldsymbol{q}})\delta(\varepsilon_{n\boldsymbol{k}} - \varepsilon_{m\boldsymbol{k}+\boldsymbol{q}} + \hbar\omega_{\nu\boldsymbol{q}}) + (N^0_{\nu\boldsymbol{q}} + 1 - f^0_{m\boldsymbol{k}+\boldsymbol{q}})\delta(\varepsilon_{n\boldsymbol{k}} - \varepsilon_{m\boldsymbol{k}+\boldsymbol{q}} - \hbar\omega_{\nu\boldsymbol{q}})], \quad (4)$$

where $\hbar\omega_{\nu\boldsymbol{q}}$ is the phonon energy, $N^0_{\nu\boldsymbol{q}}$ ($f^0_{m\boldsymbol{k}+\boldsymbol{q}}$) is the Bose-Einstein (Fermi-Dirac) distribution, and $g_{nm\nu}(\boldsymbol{k},\boldsymbol{q})$ is the e-ph coupling matrix element corresponding to electron scattering from band n at $\boldsymbol{k}$ to band m at $\boldsymbol{k}+\boldsymbol{q}$ by phonon ν with $\boldsymbol{q}$. Here, a Wannier-Fourier interpolation method [29] is used to obtain numerical results of e-ph coupling.

In Figs. 4(a) and 4(b), we plot the $\boldsymbol{q}$-dependent average e-ph coupling matrix element of all 42 phonon modes for electron scattering from the DNS band at the A point of the BZ. It is found that the e-ph interactions are indeed ultraweak and the average coupling matrix element is about several meV, which is 2 orders of magnitude smaller than that of graphene [38]. Similar results are obtained at the other momenta [15]. The calculated electron linewidths

for the occupied DNS band of anionic electrons and for an unoccupied band of atomic bound electrons are shown in Fig. 4(c). Strikingly, the former is much smaller than the latter over the entire BZ. Correspondingly, the scattering rate of anionic electrons at low energy is much lower than that of atomic bound electrons at high energy, as shown in Fig. 4(d). As a result, the plasmon relaxation time is ~130 fs (at $T = 300$ K) [57] for the DNS states, even longer than that of graphene plasmons at high carrier density [31,61]. The low electron scattering of graphene is mostly contributed to by the low DOS near E_F, while the carrier doping will inevitably result in a rapid increase of scattering rate [31,38]. In contrast, the ultraweak *e*-ph coupling and nearly constant DOS exist in a wide energy range for Ba_3CrN_3, leading to a low phonon scattering rate over a large range of doping [Fig. 4(d)].

In conclusion, we demonstrate an ADP excited by a DNS state in a 1D electride, which exhibits an anomalous density-independent frequency, intensity, and damping. It can help realize stable functionalities of plasmons in changeable environments, enable a low-frequency plasmon with high intensity, and lead to long-lived plasmons at high carrier density.

The authors thank L. Kang and X. Zhang for helpful discussions. The authors at Beijing acknowledge the support from the Science Challenge Project (Grant No. TZ2016003), MOST of China (Grants No. 2017YFA0303404 and No. 2016YFA0301001), NSFC (Grants No. 11574024, No. 11674188, and No. 11334006), and NSAF U1930402. F. L. acknowledge the support from US-DOE (Award No. DE-FG02-04ER46148). Part of the calculations were performed at Tianhe2-JK at CSRC.

J. W. and X. S. contributed equally to this work.

*fliu@eng.utah.edu
†bing.huang@csrc.ac.cn

[1] S. A. Maier, *Plasmonics: Fundamentals and Applications* (Springer, New York, 2007).
[2] W. L. Barnes, A. Dereux, and T. W. Ebbesen, Surface plasmon subwavelength optics, Nature (London) **424**, 824 (2003).
[3] E. Ozbay, Plasmonics: Merging photonics and electronics at nanoscale dimensions, Science **311**, 189 (2006).
[4] D. K. Gramotnev and S. I. Bozhevolnyi, Plasmonics beyond the diffraction limit, Nat. Photonics **4**, 83 (2010).
[5] S. Lal, S. Link, and N. J. Halas, Nano-optics from sensing to waveguiding, Nat. Photonics **1**, 641 (2007).
[6] H. A. Atwater and A. Polman, Plasmonics for improved photovoltaic devices, Nat. Mater. **9**, 205 (2010).
[7] C. Clavero, Plasmon-induced hot-electron generation at nanoparticle/metal-oxide interfaces for photovoltaic and photocatalytic devices, Nat. Photonics **8**, 95 (2014).
[8] F. Bonaccorso, Z. Sun, T. Hasan, and A. C. Ferrari, Graphene photonics and optoelectronics, Nat. Photonics **4**, 611 (2010).
[9] F. H. L. Koppens, D. E. Chang, and F. J. G. de Abajo, Graphene plasmonics: A platform for strong light-matter interactions, Nano Lett. **11**, 3370 (2011).
[10] L. Ju, B. Geng, J. Horng, C. Girit, M. Martin, Z. Hao, H. A. Bechtel, X. Liang, A. Zettl, Y. R. Shen, and F. Wang, Graphene plasmonics for tunable terahertz metamaterials, Nat. Nanotechnol. **6**, 630 (2011).
[11] A. N. Grigorenko, M. Polini, and K. S. Novoselov, Graphene plasmonics, Nat. Photonics **6**, 749 (2012).
[12] Z. Fei *et al.*, Gate-tuning of graphene plasmons revealed by infrared nanoimaging, Nature (London) **487**, 82 (2012).
[13] J. Chen *et al.*, Optical nano-imaging of gate-tunable graphene plasmons, Nature (London) **487**, 77 (2012).
[14] D. Rodrigo, O. Limaj, D. Janner, D. Etezadi, F. J. G. de Abajo, V. Pruneri, and H. Altug, Mid-infrared plasmonic biosensing with graphene, Science **349**, 165 (2015).
[15] See Supplemental Material at http://link.aps.org/supplemental/10.1103/PhysRevLett.123.206402 for details of three different 3D topological semimetals (DNP, DNL, and DNS) and their plasmon excitation derivations, the proof of density dependence of plasmon intensity, computational methods, electronic and plasmonic properties of Ba_3CrN_3 and Sr_3CrN_3, discussions of symmetry protection and topological invariant of nodal surface, and *e*-ph coupling calculation tests of Ba_3CrN_3, which also includes Refs. [16–38].
[16] S. D. Sarma and E. H. Hwang, Collective Modes of the Massless Dirac Plasma, Phys. Rev. Lett. **102**, 206412 (2009).
[17] J.-W. Rhim and Y. B. Kim, Anisotropic density fluctuations, plasmons, and Friedel oscillations in nodal line semimetal, New J. Phys. **18**, 043010 (2016).
[18] D. Pines and P. Nozieres, *The Theory of Quantum Liquids* (Benjamin, New York, 1966).
[19] G. Kresse and J. Furthmüller, Efficiency of *ab-initio* total energy calculations for metals and semiconductors using a plane-wave basis set, Comput. Mater. Sci. **6**, 15 (1996).
[20] G. Kresse and J. Furthmüller, Efficient iterative schemes for *ab initio* total-energy calculations using a plane-wave basis set, Phys. Rev. B **54**, 11169 (1996).
[21] P. E. Blöchl, Projector augmented-wave method, Phys. Rev. B **50**, 17953 (1994).
[22] J. P. Perdew, K. Burke, and M. Ernzerhof, Generalized Gradient Approximation Made Simple, Phys. Rev. Lett. **77**, 3865 (1996).
[23] M. G. Barker, M. J. Begley, P. P. Edwards, D. H. Gregory, and S. E. Smith, Synthesis and crystal structures of the new ternary nitrides Sr_3CrN_3 and Ba_3CrN_3, J. Chem. Soc. Dalton Trans. **1996**, 1 (1996).
[24] N. Marzari and D. Vanderbilt, Maximally localized generalized Wannier functions for composite energy bands, Phys. Rev. B **56**, 12847 (1997).
[25] I. Souza, N. Marzari, and D. Vanderbilt, Maximally localized Wannier functions for entangled energy bands, Phys. Rev. B **65**, 035109 (2001).
[26] A. L. Fetter and J. D. Walecka, *Quantum Theory of Many-Particle Systems* (McGraw-Hill, San Francisco, 1971).
[27] G. D. Mahan, *Many-Particle Physics* (Plenum Press, New York, 1990).

[28] F. Giustino, M. L. Cohen, and S. G. Louie, Electron-phonon interaction using Wannier functions, Phys. Rev. B **76**, 165108 (2007).

[29] S. Poncé, E. R. Margine, C. Verdi, and F. Giustino, EPW: Electron-phonon coupling, transport and superconducting properties using maximally localized Wannier functions, Comput. Phys. Commun. **209**, 116 (2016).

[30] P. Giannozzi, S. Baroni, N. Bonini, M. Calandra, R. Car, C. Cavazzoni, D. Ceresoli, G. L. Chiarotti, and M. Cococcioni, QUANTUM ESPRESSO: A modular and open-source software project for quantum simulations of materials, J. Phys. Condens. Matter **21**, 395502 (2009).

[31] H. Yan, T. Low, W. Zhu, Y. Wu, M. Freitag, X. Li, F. Guinea, P. Avouris, and F. Xia, Damping pathways of mid-infrared plasmons in graphene nanostructures, Nat. Photonics **7**, 394 (2013).

[32] G. X. Ni *et al.*, Fundamental limits to graphene plasmonics, Nature (London) **557**, 530 (2018).

[33] D. A. Bandurin *et al.*, Resonant terahertz detection using graphene plasmons, Nat. Commun. **9**, 5392 (2018).

[34] S. A. Parameswaran, A. M. Turner, D. P. Arovas, and A. Vishwanath, Topological order and absence of band insulators at integer filling in non-symmorphic crystals, Nat. Phys. **9**, 299 (2013).

[35] H. Watanabe, H. C. Po, M. P. Zaletel, and A. Vishwanath, Filling-Enforced Gaplessness in Band Structures of the 230 Space Groups, Phys. Rev. Lett. **117**, 096404 (2016).

[36] R. Chen, H. C. Po, J. B. Neaton, and A. Vishwanath, Topological materials discovery using electron filling constraints, Nat. Phys. **14**, 55 (2018).

[37] S. A. Parameswaran, Topological "Luttinger" invariants protected by non-symmorphic symmetry in semimetals, arXiv:1508.01546.

[38] K. M. Borysenko, J. T. Mullen, E. A. Barry, S. Paul, Y. G. Semenov, J. M. Zavada, M. B. Nardelli, and K. W. Kim, First-principles analysis of electron-phonon interactions in graphene, Phys. Rev. B **81**, 121412(R) (2010).

[39] C.-K. Chiu, J. C. Y. Teo, A. P. Schnyder, and S. Ryu, Classification of topological quantum matter with symmetries, Rev. Mod. Phys. **88**, 035005 (2016).

[40] N. P. Armitage, E. J. Mele, and A. Vishwanath, Weyl and Dirac semimetals in three-dimensional solids, Rev. Mod. Phys. **90**, 015001 (2018).

[41] A. A. Burkov, M. D. Hook, and L. Balents, Topological nodal semimetals, Phys. Rev. B **84**, 235126 (2011).

[42] H. Weng, X. Dai, and Z. Fang, Topological semimetals predicted from first-principles calculations, J. Phys. Condens. Matter **28**, 303001 (2016).

[43] Z. Yan, P.-W. Huang, and Z. Wang, Collective modes in nodal line semimetals, Phys. Rev. B **93**, 085138 (2016).

[44] A. Politano, G. Chiarello, B. Ghosh, K. Sadhukhan, C.-N. Kuo, C. S. Lue, V. Pellegrini, and A. Agarwal, 3D Dirac Plasmons in the Type-II Dirac Semimetal $PtTe_2$, Phys. Rev. Lett. **121**, 086804 (2018).

[45] Q.-F. Liang, J. Zhou, R. Yu, Z. Wang, and H. Weng, Node-surface and node-line fermions from nonsymmorphic lattice symmetries, Phys. Rev. B **93**, 085427 (2016).

[46] W. Wu, Y. Liu, S. Li, C. Zhong, Z.-M. Yu, X.-L. Sheng, Y. X. Zhao, and S. A. Yang, Nodal surface semimetals: Theory and material realization, Phys. Rev. B **97**, 115125 (2018).

[47] J. L. Dye, Electrides: Ionic salts with electrons as the anions, Science **247**, 663 (1990).

[48] J. L. Dye, Electrons as anions, Science **301**, 607 (2003).

[49] S. Matsuishi, Y. Toda, M. Miyakawa, K. Hayashi, T. Kamiya, M. Hirano, I. Tanaka, and H. Hosono, High-density electron anions in a nanoporous single crystal: $[Ca_24Al_28O_64]^{4+}(4e^-)$, Science **301**, 626 (2003).

[50] K. Lee, S. W. Kim, Y. Toda, S. Matsuishi, and H. Hosono, Dicalcium nitride as a two-dimensional electride with an anionic electron layer, Nature (London) **494**, 336 (2013).

[51] L. A. Burton, F. Ricci, W. Chen, G.-M. Rignanese, and G. Hautier, High-throughput identification of electrides from all known inorganic materials, Chem. Mater. **30**, 7521 (2018).

[52] M. Hirayama, S. Matsuishi, H. Hosono, and S. Murakami, Electrides as a New Platform of Topological Materials, Phys. Rev. X **8**, 031067 (2018).

[53] H. Buljan, M. Jablan, and M. Soljačić, Damping of plasmons in graphene, Nat. Photonics **7**, 346 (2013).

[54] A. Woessner, M. B. Lundeberg, Y. Gao, A. Principi, P. A. González, M. Carrega, K. Watanabe, T. Taniguchi, G. Vignale, M. Polini, J. Hone, R. Hillenbrand, and F. H. L. Koppens, Highly confined low-loss plasmons in graphene-boron nitride heterostructures, Nat. Mater. **14**, 421 (2015).

[55] X. Zeng, S. Zhao, Z. Li, and J. Yang, Electron-phonon interaction in a Ca_2N monolayer: Intrinsic mobility of electrene, Phys. Rev. B **98**, 155443 (2018).

[56] Z. F. Wang and F. Liu, Self-Assembled Si(111) Surface States: 2D Dirac Material for THz Plasmonics, Phys. Rev. Lett. **115**, 026803 (2015).

[57] The calculated electron scattering rate by Eq. (4) [red or blue dots in Fig. 4(d)] is not the true plasmon damping rate due to the transport factor (see Refs. [27,58] for details). Using the methods in Refs. [27,59,60], we have calculated the phonon-assisted plasmon damping rate for Ba_3CrN_3, as shown in Fig. 4(d) (black triangles). The resulting plasmon lifetime is longer than the electron relaxation time. Most importantly, however, is that the main conclusion, i.e., the phonon-assisted plasmon damping being independent of carrier densities, is drawn consistently.

[58] A. Principi, M. Carrega, M. B. Lundeberg, A. Woessner, F. H. L. Koppens, G. Vignale, and M. Polini, Plasmon losses due to electron-phonon scattering: The case of graphene encapsulated in hexagonal boron nitride, Phys. Rev. B **90**, 165408 (2014).

[59] D. Novko, Dopant-induced plasmon decay in graphene, Nano Lett. **17**, 6991 (2017).

[60] A. M. Brown, R. Sundararaman, P. Narang, W. A. Goddard III, and H. A. Atwater, Non-radiative plasmon decay and hot carrier dynamics: Effects of phonons, surfaces and geometry, ACS Nano **10**, 957 (2016).

[61] Although the relaxation time of 130 fs is not so long compared to that of a graphene plasmon at a low carrier density (e.g., see Refs. [32,33]), it can be maintained over a large range of carrier concentrations; i.e., it is indeed longer than graphene plasmon at a high carrier density (e.g., 20 fs in Ref. [31]). The phonon-assisted damping can, in principle, be ultralow because of the weak electron-phonon coupling for anionic electrons. The non-negligible value of phonon scattering in our system, however, is due to the high DOS of the nodal-surface state.